# The average and local structure of TiVCrNbD$_x$ ($x = 0, 2.2, 8$) from total scattering and neutron spectroscopy

Magnus M. Nygård[a], Øystein S. Fjellvåg[a], Magnus H. Sørby[a,*], Kouji Sakaki[b], Kazutaka Ikeda[c], Jeff Armstrong[d], Ponniah Vajeeston[e], Wojciech A. Sławiński[f], Hyunjeong Kim[b], Akihiko Machida[g], Yumiko Nakamura[b], Bjørn C. Hauback[a]

[a] Institute for Energy Technology, Department for Neutron Materials Characterization, P.O. Box 40, NO-2027 Kjeller, Norway
[b] National Institute of Advanced Industrial Science and Technology, AIST West, 16-1 Onogawa, Tsukuba, Ibaraki, 305-8569, Japan
[c] Institute of Materials Structure Science, High Energy Accelerator Research Organization (KEK), Tsukuba, Ibaraki 305-0801, Japan
[d] ISIS Facility, Rutherford Appleton Laboratory, Harwell Campus, Didcot, Oxfordshire OX11 0QX, United Kingdom
[e] Centre for Materials Science and Nanotechnology, Department of Chemistry, University of Oslo, P.O. Box 1033, Oslo NO-0315, Norway
[f] Faculty of Chemistry, University of Warsaw, Pasteura 1, Warsaw PL-02-093, Poland
[g] National Institutes for Quantum and Radiological Science and Technology, 1-1-1, Kouto, Sayo-cho, Sayo-gun, Hyōgo, 679-5148, Japan

## ARTICLE INFO

## ABSTRACT

The volumetric hydrogen density of 160 kg H/m$^3$ in TiVCrNbH$_8$ is among the highest for interstitial hydrides, but the reported reversible capacity is only about 2/3 of the full theoretical capacity at room temperature. In the present work we have investigated the local structure in TiVCrNbD$_x$, $x = 0$, 2.2, 8 with the aim to unravel how the remaining sites can be destabilized with respect to hydrogen/deuterium occupation using total scattering measurements and Reverse Monte Carlo (RMC) structure modelling. Our analysis indicates that the partially desorbed deuteride ($x = 2.2$) adopts a body-centred tetragonal structure ($I4/mmm$) where the deuterium atoms occupy both tetrahedral and octahedral interstices with low occupancies. There is a significantly higher portion of occupied sites with nearest-neighbour metals with low valence-electron concentration $VEC$. This observation is used to motivate strategies for further destabilization of the hydride. Inelastic neutron scattering (INS) and density functional theory (DFT) calculations indicate that the vibrational density of states is very diverse in TiVCrNbH$_{2.4}$, and it is suggested that the hydrogen atoms might be mobile between nearby interstices.

© 2020 Acta Materialia Inc. Published by Elsevier Ltd.

## 1. Introduction

An environmentally benign energy vector becomes imperative with an increasing share of the global energy distribution from renewable energy technologies. Hydrogen has the potential to fill this need, but safe and efficient storage remains a challenge [1]. This is due to the very low density of gaseous hydrogen at ambient conditions. One promising solution is to store hydrogen in the solid-state using metal hydrides. With this approach it is possible to achieve much higher volumetric hydrogen densities than in commercial gas tanks where the hydrogen is compressed to 700 bar H$_2$. Many different metal hydrides have been proposed in the literature, but none of these are currently able to fulfill all the requirements of an ideal hydrogen storage material. Complex hydrides excel in terms of gravimetric hydrogen densities reach-

ing values as high as 18.4 wt.% in LiBH$_4$. Unfortunately, they are often subject to non-reversibility during hydrogen sorption [2–4]. Mg-based metal hydrides can also reach high gravimetric hydrogen densities, e.g. 7.6 wt.% in MgH$_2$. As Mg is an abundant element these materials are often cheap, but they suffer from unfavorable kinetics and thermodynamics at ambient conditions [5]. Intermetallic hydrides formed from alloys of type AB, AB$_2$, AB$_5$, etc., have modest gravimetric hydrogen densities, such as 1.37 wt.% in LaNi$_5$H$_6$ or 1.89 wt.% in TiFeH$_2$. Their main drawbacks include degradation after repeated hydrogen absorption/desorption cycling, surface passivation and slow hydrogen sorption kinetics [1,6–9]. Some of these issues can be mitigated if small amounts of either A, B, or both is substituted with carefully chosen elements [9–12].

Recently, this alloying strategy has been taken to its extreme in a novel materials class known as high-entropy alloys (HEAs). This is a multi-principal element approach where the alloy contains four or more elements mixed together in near equimolar compositions. These materials tend to form single-phase solid

* Corresponding author.
E-mail address: magnus.sorby@ife.no (M.H. Sørby).

solutions with simple structures such as body-centred cubic (bcc) and cubic close-packed (ccp) [13]. As a consequence, the different elements are randomly distributed over a single crystallographic site causing a wide diversity of local atomic arrangements. Several HEAs have been reported to form metal hydrides in which the hydrogen atoms occupy the tetrahedral and/or octahedral interstices in a body-centred tetragonal (bct) or face-centred cubic (fcc) lattice [14–20]. Usually the thermodynamics are unfavorable for applications at ambient conditions [16–18], but it has recently been demonstrated that the metal hydrides are destabilized with increasing valence-electron concentration (VEC) in the HEA [21]. Based upon this insight, reversible room temperature (RT) hydrogen storage have been realized in the HEA TiVCrNbH$_8$ (VEC = 5.0) and the C14 Laves-phase TiCrMnFeNiZrH$_6$ (VEC = 6.4) [21,22]. The volumetric hydrogen density achieved in TiVCrNbH$_8$ is the highest reported for any interstitial hydride, namely 160 kg H/m$^3$. Interestingly, the reversible hydrogen storage capacity of 1.96 wt.% H in TiVCrNbH$_8$ is just 61.3% of the theoretical full capacity of 3.20 wt.%. This is indicative of certain more stable sites where the remaining hydrogen atoms are trapped. These sites must be destabilized if the full hydrogen storage capacity in TiVCrNbH$_8$ should become available at RT. It is possible that this can be achieved by finely tuning the chemical composition of the HEA. In this context it would be beneficial to know whether there are any preferred metallic environments surrounding the hydrogen atoms that are trapped inside the structure at RT.

This paper presents a detailed investigation of the local short-range order (SRO) for TiVCrNbD$_x$, x = 0, 2.2, 8 using Reverse Monte Carlo (RMC) structure modelling from total scattering measurements [23]. Total scattering extends regular diffraction and involve extra rigorous measurements to obtain an accurate assessment of both the Bragg and diffuse scattering from the sample. Previous total scattering investigations indicated that deuterium has a preferrence for occupying sites surrounded by much Ti in deuterides formed from Ti$_{0.45}$Cr$_{0.35}$Mo$_{0.20}$ [24]. However, this result was obtained by peak fitting rather than RMC modelling, and thus, a more accurate assessment of the local structure is obtained in this work. The hydrogen vibrations and local bonding mechanism are also elucidated from high-resolution inelastic neutron scattering (INS) measurements. These are discussed and compared with density functional theory (DFT) calculations and the RMC structure models.

## 2. Experimental

### 2.1. Synthesis.

Alloys with the composition TiVCrNb were synthesised from lumps of Ti, Cr, Nb (Goodfellow, 99.99% metals basis) and V (Goodfellow, 99.6% metals basis) by arc melting under Ar atmosphere. The alloys were melted in batches of 1.86(1) g. These were turned and remelted six times to enhance homogeneity. The mass losses during arc melting were in all cases measured below 0.6 wt.%. Thus, the final compositions can be considered as very close to the nominal.

About one third of the as cast alloy was crushed to a fine powder using a hammer and anvil. Another third of the material was sealed under Ar in a stainless steel autoclave and connected to an in-house built Sieverts apparatus [25] equipped with a Vacuubrand diaphragm vacuum pump. A partially hydrogenated material was obtained by the following synthesis. The material was heated to 352(2) °C under dynamic vacuum for 2 h for activation. The sample was subsequently cooled to RT where hydrogen loading was performed in a direct gas-solid-state reaction. The final pressure was stable at 33.9(3) bar H$_2$, and the composition was measured to TiVCrNbH$_{7.68(2)}$ by manometric means. The sample was then heated to 99.0(4) °C and exposed to dynamic vacuum for 3 h until

the vacuum was at ∼ 2 × 10$^{-6}$ mbar. This indicates that hydrogen desorption has finished. Hydrogen gas loading was then repeated at RT and the reversible capacity determined to H/M = 1.214(7). The loading cycle was repeated one more time with no significant change in the reversible capacity. A partially hydrogenated material was finally obtained by repeating the heating and evacuation procedure described above. The remaining one third of the as cast alloy was exposed to an identical treatment with deuterium ($^2$H, purity 99.6%) instead of natural hydrogen. The composition of the fully deuterated material and the reversible capacity was determined manometrically to TiVCrNbD$_{7.65(7)}$ and D/M = 1.26(3), respectively. All sample handling was from this point performed in an MBraun Unilab glovebox with purified Ar atmosphere (< 1 ppm O$_2$ and H$_2$O).

A deactivated dideuteride was also obtained by the following synthesis. Part of the partially deuterated material obtained above was sealed in a stainless steel autoclave and reconnected to the Sieverts apparatus. Deuterium gas loading was performed as described above and the final composition was measured to TiVCrNbD$_{7.82(1)}$. To prevent outgassing of deuterium the sample was cooled to −196 °C by submerging the stainless steel autoclave in a liquid N$_2$ bath. During cooling the sample was kept under deuterium gas pressure. The sample was then quickly removed from the autoclave and placed in acetone where it was grounded to a fine powder. The latter step served to passivate the surfaces of the dideuteride particles, and thereby preventing D desorption.

### 2.2. Thermal analysis.

Thermogravimetric differential scanning calorimitry (TG/DSC) was measured with a heat flux type Netzsch STA 449 F3 Jupiter apparatus. The samples were confined inside Al$_2$O$_3$ crucibles equipped with pierced lids and heated to 600 °C at 10 °C/min. The measurements were conducted under flowing Ar at 50 mL/min.

### 2.3. Sieverts measurements.

The powdered alloys were placed inside a stainless-steel autoclave for the pressure-composition isotherm (PCI) measurements. The autoclave was heated to 150 °C and evacuated by rotary pump for more than 2 h. PCIs were then measured during absorption/desorption at three different temperatures so that the absorption/desorption enthalpy and entropy could be evaluated. Separate measurements were conducted with hydrogen and deuterium gas.

### 2.4. X-ray and neutron total scattering measurements.

Powder neutron diffraction (PND) was measured with the NOVA instrument at Japan Proton Accelerator Research Complex (J-PARC) in Ibaraki Prefecture, Japan. The samples were loaded into 6 mm diameter cylindrical V$_{96}$Ni$_4$ alloy containers under He atmosphere. Each sample was measured for 3.5 h under ambient conditions. Measurements were also made of an empty sample container, a V rod and the empty instrument. This allowed us to perform background subtraction and data correction by standard means [26] to obtain the total scattering structure factor F(Q) and its Fourier transform, the pair distribution function (PDF), G(r) defined as:

$$G(r) = \sum_{i=1}^{N} \sum_{j=1}^{N} c_i c_j \bar{b}_i \bar{b}_j \left[ g_{ij}(r) - 1 \right] \qquad (1)$$

where $\{c_i\}_{i=1}^{N}$ and $\left\{ \bar{b}_i \right\}_{i=1}^{N}$ are the concentrations and coherent bound scattering lengths of the N chemical species present in the system, respectively [27]. $g_{ij}(r)$ are the partial PDFs defined as:

$$g_{ij}(r) = \frac{1}{\rho_j} \frac{n_{ij}(r)}{4\pi r^2 dr} \qquad (2)$$

where $\rho_j = c_j\rho_0$, $\rho_0$ is the average number density of the material and $n_{ij}(r)$ is the number of atoms of type $j$ between $r$ and $r + dr$ from an atom of type $i$. Thus, $g_{ij}(r)$ shows the distribution of interatomic distances between atoms of type $i$ and $j$. Additionally, the differential correlation function $D(r)$ is obtained as $D(r) = 4\pi r\rho_0 G(r)$.

Synchrotron radiation powder X-ray diffraction (SR-PXD) was measured at the BL22-XU beamline of SPring-8 in Hyōgo Prefecture, Japan [28]. The beamline is equipped with a Rigaku R-AXIS V detector and the wavelength was $\lambda = 0.1778$ Å. The samples were placed inside 1.0 mm diameter kapton capillaries with wall thickness 0.05 mm. The exposure times were in all cases 30 s. An empty capillary was also measured so that background subtraction and data correction could be performed using the program GudrunX [29]. Thus, X-ray equivalents of the total scattering functions described above were obtained.

Crystallographic analysis was performed with both SR-PXD and PND data simultaneously using the Rietveld method in the General Structure Analysis System (GSAS) [30,31]. The background was fitted by a 12th order shifted-Chebyshev polynomial, and the SR-PXD peaks were modelled by a Thompson–Cox–Hastings pseudo-Voigt function [32]. The PND peaks were modelled by a pseudo-Voigt function convoluted with the Ikeda–Carpenter function [33]. The Debye–Waller factors were also refined, but for the metals they were constrained to be equal.

### 2.5. Reverse Monte Carlo (RMC) modelling.

In the RMC technique a three dimensional structure model is constructed from experimentally observed data. In the case of a crystalline material, the initial model is a supercell of the crystallographic unit obtained from a Rietveld refinement. The theoretical function, e.g. $G(r)$, from this configuration of atoms is calculated and compared with the experimentally obtained function. The atoms within the configuration is then allowed to translate and swap places. For each move the new agreement with the experimental data $\chi_j^2$ is calculated as:

$$\chi_j^2 = \sum_{i=1}^{M} \frac{(f_{meas}(x_i) - f_{calc,j}(x_i))^2}{A \cdot \sigma(x_i)} \tag{3}$$

where $f_{meas}(x_i)$ is the experimental function with uncertainty $\sigma(x_i)$ at point $x_i$ and $f_{calc,j}(x_i)$ the corresponding function calculated from the model after move $j$ has been implemented. $A$ is a user defined constant that is used to change the relative weighting of the different functions. If $\chi_j^2 \leq \chi_{j-1}^2$ the move is always accepted. If $\chi_j^2 > \chi_{j-1}^2$ it is accepted with probability $\exp(-0.5 \cdot (\chi_j^2 - \chi_{j-1}^2))$. In principle, any technique for which a theoretical pattern can be calculated from the structure model could be included into the RMC process. In the present work, a combination of neutron and X-ray total scattering measurements is used. This is necessary due to the low X-ray scattering intensity from D atoms with respect to the metals and *vice versa* for neutrons. This also ensures good contrast between all the metals.

The RMC modelling was in the present work done with the development version of RMCProfile v7 which will succeed the current version RMCProfile v6 [34]. A total of eight different functions, four for each probe, were included in the RMC procedure. These are $F(Q)$, $G(r)$, $D(r)$ and the Bragg peak intensities. The dimension of the starting configurations were chosen so that $G(r)$ and $D(r)$ could be calculated up to 30 Å. Thus, the models of the alloy, partially deuterated and fully deuterated materials contain $20 \times 20 \times 20$ (16,000 atoms), $19 \times 19 \times 19$ (21,310 atoms) and $14 \times 14 \times 14$ (32,928 atoms) unit cells, respectively. Translation and swap moves were attempted with equal probability during the simulations. The maximum translation distance was restricted to

0.10 Å. The atoms were constrained to not move closer together than the predefined cut-off distance of 2.28 Å in TiVCrNb, 1.32 Å in TiVCrNbD$_{2.2}$, and 1.38 Å in TiVCrNbD$_8$. These values were taken for each simulation as the $r$-value where the first interatomic distance peak is seen in the experimental $G(r)$. No further chemical knowledge or constrains were imposed on the models. The relative weighting of the different datasets were decided by trial and error so that a good fit was obtained for all included functions. A total of 10 simulations with different starting configurations were done for all the considered systems.

### 2.6. Inelastic neutron scattering (INS).

High-resolution INS measurements were conducted at the indirect-geometry spectrometer TOSCA at ISIS Neutron and Muon Source, Rutherford Appleton Laboratory in the United Kingdom [35,36]. 5 g samples of the alloy and the partially desorbed hydride were placed inside flat Al cells with cross-sectional area $4.0 \times 4.8\,cm^2$ and thickness 0.5 mm. The cross-section of the beam was $4.0 \times 4.0\,cm^2$. The INS spectra were collected below $-258\,°C$ using a closed-cycle He refrigerator. This was done to minimize the contribution of the Debye–Waller factor. 10 g of the partially desorbed hydride was also placed inside a stainless steel cylinder with diameter 12.5 mm and height 6.0 cm. Hydrogen gas loading was performed by exposing the sample to 35 bar H$_2$ at 127 °C until no change could be observed in the INS spectrum. The sample was then cooled to *RT* where the INS spectrum was recorded under hydrogen gas pressure.

### 2.7. Density functional theory (DFT) calculations.

Phonon spectra were calculated by DFT to generate *in silico* spectra for comparison with experimental INS equivalents. For the fully hydrogenated compound, the binary hydrides with CaF$_2$-type structures were investigated. For TiVCrNbH$_{2.4}$, a $2 \times 2 \times 2$ supercell with nominal composition TiVCrNbH$_{2.25}$ with random structure approximation was utilized. In this simulation, the Ti, V, Cr and Nb atoms are swapped randomly to find the minimum energy configuration. The phonon calculation was carried out only for the final, low energy configuration.

Total energies were calculated by the projected-augmented plane-wave (PAW) implementation of the Vienna *ab initio* simulation package (VASP) [37,38]. All these calculations were made with the Perdew–Burke–Ernzerhof (PBE) [39] exchange correlation functional with the Hubbard parameter correction (LDA+$U$), following the rotationally invariant form [40,41]. Effective $U$ values of 3.25 eV and 3.7 eV were used for the V-$d$ and Cr-$d$ states, respectively.

Ground-state geometries were determined by minimizing stresses and Hellman–Feynman forces using the conjugate-gradient algorithm with force convergence less than $10^{-3}$ eV/Å. Brillouin zone integration was performed with a Gaussian broadening of 0.1 eV during all relaxations. From various sets of calculations it was found that 512 **k**-points in the whole Brillouin zone for the structure with a 600 eV plane-wave cutoff were sufficient to ensure optimum accuracy in the computed results. The **k**-points were generated using the Monkhorst–Pack method with a grid size of $8 \times 8 \times 8$ for structural optimization. A similar density of **k**-points and energy cutoff were used to estimate total energy as a function of volume for all the structures considered in the present work.

A frozen phonon calculation was applied to the supercells using the phonopy program to obtain the phonon dispersion curve and phonon density of states [42]. An atomic displacement of 0.0075 Å was used with a symmetry consideration to obtain the force constants for the phonon calculations. The displacements in opposite directions along all possible axes were incorporated in the calculations to improve the precision. The force calculations were made
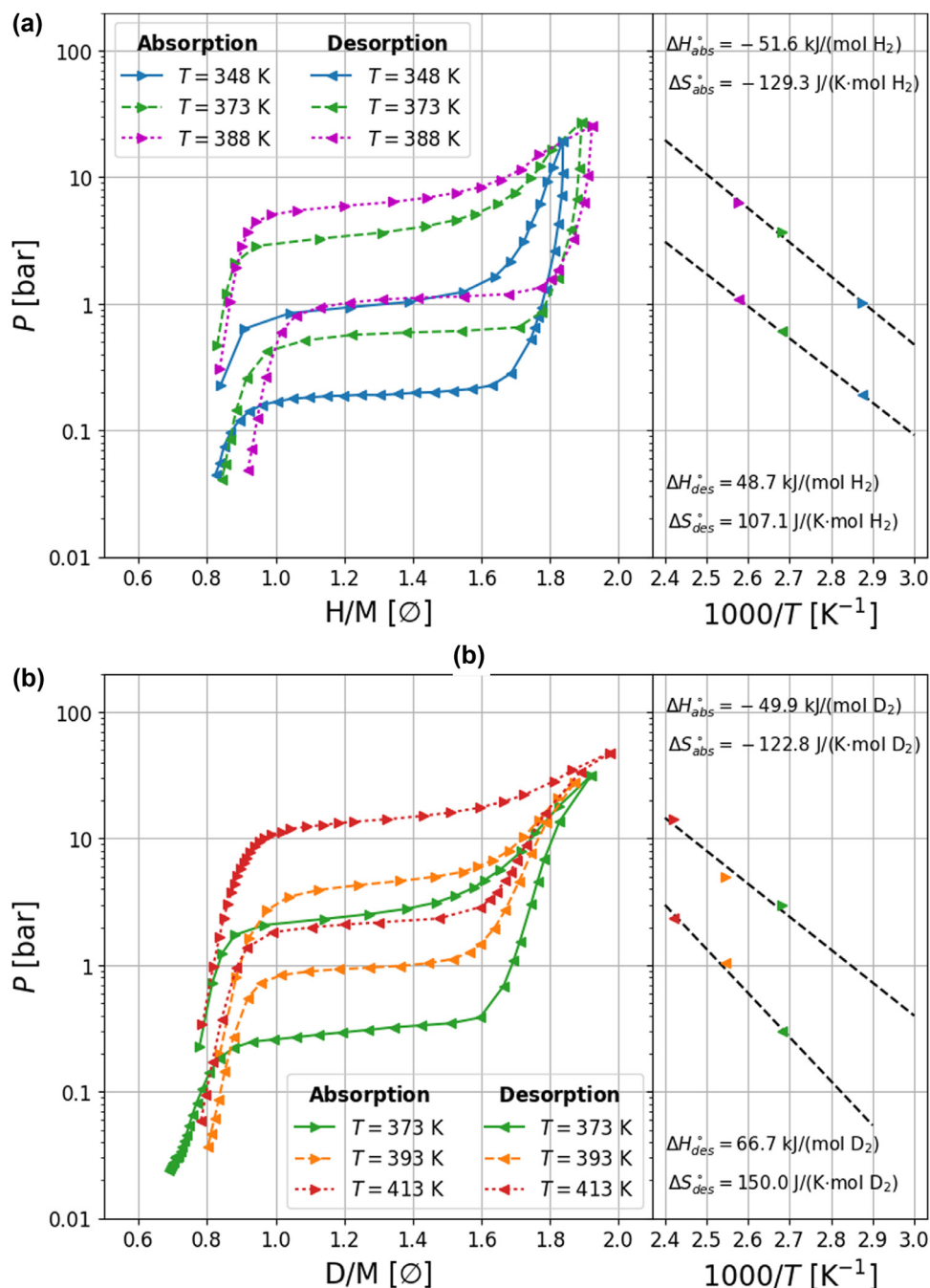
**Fig. 1.** PCIs (left) and corresponding van 't Hoff diagrams (right) for absorption and desorption of hydrogen (a) and deuterium (b) in TiVCrNb.

using the VASP code with the supercell approach (with LDA + *U* correction) and the resulting data were imported into the Phonopy program. The dynamical matrices were calculated from the force constants, and phonon density of states (PhDOS) curves were computed using the Monkhorst–Pack scheme [43]. Phonon calculation was weighted with the neutron scattering cross sections included with AbINS in the Mantid software to obtain *in silico* spectra for comparison with the experimental INS spectra. [44,45].

## 3. Results and discussion

The H and D contents of the partially hydrogenated/deuterated materials can be determined from the difference between the maximum and reversible hydrogen contents measured manometrically.

This calculation suggests that the synthesized compounds have compositions $TiVCrNbH_{2.82(3)}$ and $TiVCrNbD_{2.60(16)}$, respectively. TG/DSC data were also measured to verify these results. It was found that the compositions are lower than what was suggested from the manometric measurements, namely $TiVCrNbH_{2.44(3)}$ and $TiVCrNbD_{2.20(4)}$. A possible explanation to these discrepancies is that the maximum H and D contents are reduced from the first to the second loading cycle.

Fig. 1 shows hydrogen and deuterium pressure composition isotherms (PCIs) and the corresponding van 't Hoff diagrams for $TiVCrNbH_x$ and $TiVCrNbD_x$. The measured curves are characterized by two plateaus. The pressure at the first plateau is below the range of the pressure transducer in the Sieverts apparatus. The second is characterized by a significant level of hysteresis and a slope
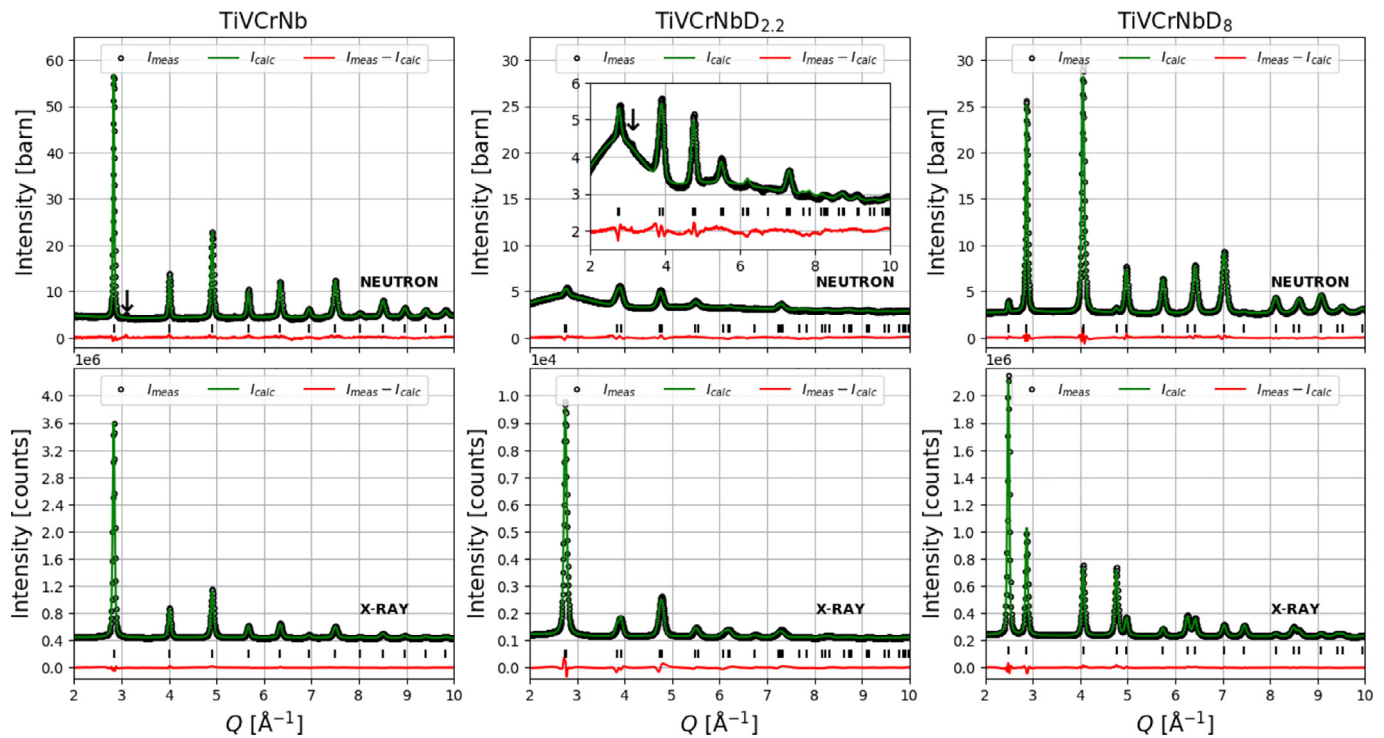
**Fig. 2.** Rietveld refinements of PND and SR-PXD patterns for TiVCrNbD$_x$, $x = 0, 2.2, 8$ at $RT$. Visible peaks corresponding to Fe are indicated by black arrows. The inset of the upper middle panel shows an enlargement of the PND fit for TiVCrNbD$_{2.2}$.

in the plateau pressure. Attempts were made to measure PCIs at $RT$, but this was not possible. Extrapolation suggests that the desorption plateau pressures are 0.01 bar and 0.002 bar for hydrogen and deuterium, respectively. These values are below the lower limit of 0.03 bar of the pressure transducer which explains why we were unable to measure the PCIs at $RT$. It is clear that the plateau pressures are higher for hydrogen in comparison with deuterium, but the shape of the curves are similar. Moreover, the final hydrogen contents of the full and partially desorbed materials are comparable. This suggests that the structures of deuterides must be the same as those of the hydrides. Thus, the hydrogenation/deuteration process can be described as

$$\alpha \rightleftharpoons \beta \rightleftharpoons \gamma \qquad (4)$$

where $\alpha$ denotes the deuterium free alloy, $\beta$ the partially deuterated system and $\gamma$ the dideuteride.

Fig. 2 presents Rietveld refinements of PND and SR-PXD patterns of TiVCrNbD$_x$, $x = 0, 2.2, 8.0$. The corresponding crystallographic information is given in Table 1. The as cast alloy ($\alpha$) is bcc ($Im\bar{3}m$), the partially deuterated material ($\beta$) is bct ($I4/mmm$) and the dideuteride ($\gamma$) has a CaF$_2$-type structure ($Fm\bar{3}m$). Extra peaks corresponding to Fe coming from the anvil where the as cast alloys were crushed can be seen in the PND patterns of both TiVCrNb and TiVCrNbD$_{2.2}$. The strongest peak for Fe is indicated by arrows in the figure. These peaks are not visible in the SR-PXD patterns, and our Rietveld refinement indicates that the amount of Fe is less than 0.3 wt.%. Thus, the contribution of this impurity to the PDF is insignificant. Notice the much lower scattering intensity with both X-rays and neutrons from TiVCrNbD$_{2.2}$ in comparison to the alloy and dideuteride. At the same time there is substantial diffuse scattering in the $Q$-range from 2.0 Å$^{-1}$ to 4.5 Å$^{-1}$ of the PND pattern. This is indicative of SRO in the deviations from the average long-range atomic structure. All octahedral and tetrahedral interstices are occupied by D with low occupancies for this material (see Table 1). The distances between these sites are summarized

**Table 1**

Crystallographic data for TiVCrNbD$_x$, $x = 0, 2.2, 8$ at $RT$. Note that Ti, V, Cr and Nb occupy the $M$-site with equal probability. Estimated standard deviations are given in parentheses.

| Compound: | | | **TiVCrNb** | | | |
|---|---|---|---|---|---|---|
| Space group: | | | $Im\bar{3}m$ | | | |
| Lattice parameter, $a$: | | | 3.13228(7) Å | | | |
| Unit cell volume, $V_0$: | | | 30.731(12) Å$^3$ | | | |
| Mass density, $\rho$: | | | 6.585 g/cm$^3$ | | | |
| Number density, $\rho_0$: | | | 0.0651 atoms/Å$^3$ | | | |

| Atom | Site | $x$ | $y$ | $z$ | $U_{iso}$ | Occupancy |
|---|---|---|---|---|---|---|
| $M$ | 2a | 0 | 0 | 0 | 0.00932(5) | 1.0 |

| Compound: | | | **TiVCrNbD$_{2.2}$** | | | |
|---|---|---|---|---|---|---|
| Space group: | | | $I4/mmm$ | | | |
| Lattice parameter, $a$: | | | 3.2048(2) Å | | | |
| Lattice parameter, $c$: | | | 3.2747(3) Å | | | |
| Unit cell volume, $V_0$: | | | 33.635(6) Å$^3$ | | | |
| Mass density, $\rho$: | | | 6.127 g/cm$^3$ | | | |
| Number density, $\rho_0$: | | | 0.0924 atoms/Å$^3$ | | | |

| Atom | Site | $x$ | $y$ | $z$ | $U_{iso}$ | Occupancy |
|---|---|---|---|---|---|---|
| $M$ | 2a | 0 | 0 | 0 | 0.022(2) | 1.0 |
| D | 2b | 0 | 0 | 1/2 | 0.0368(9) | 0.105(1) |
| D | 4c | 1/2 | 0 | 0 | 0.1198(11) | 0.081(4) |
| D | 4d | 1/2 | 0 | 1/4 | 0.0561(16) | 0.042(4) |
| D | 8j | 0.2118(7) | 0 | 1/2 | 0.0216(7) | 0.051(8) |

| Compound: | | | **TiVCrNbD$_8$** | | | |
|---|---|---|---|---|---|---|
| Space group: | | | $Fm\bar{3}m$ | | | |
| Lattice parameter, $a$: | | | 4.37800(3) Å | | | |
| Unit cell volume, $V_0$: | | | 83.912(2) Å$^3$ | | | |
| Mass density, $\rho$: | | | 5.142 g/cm$^3$ | | | |
| Number density, $\rho_0$: | | | 0.1430 atoms/Å$^3$ | | | |

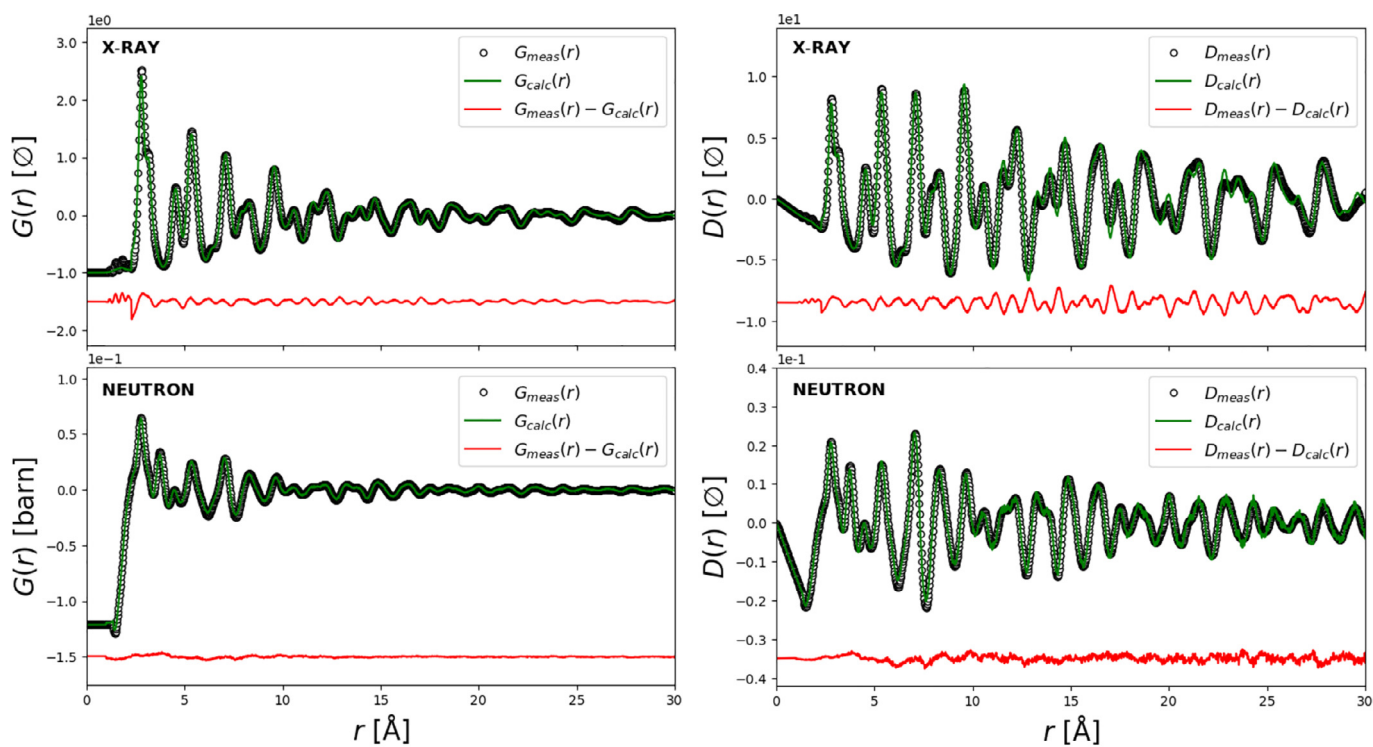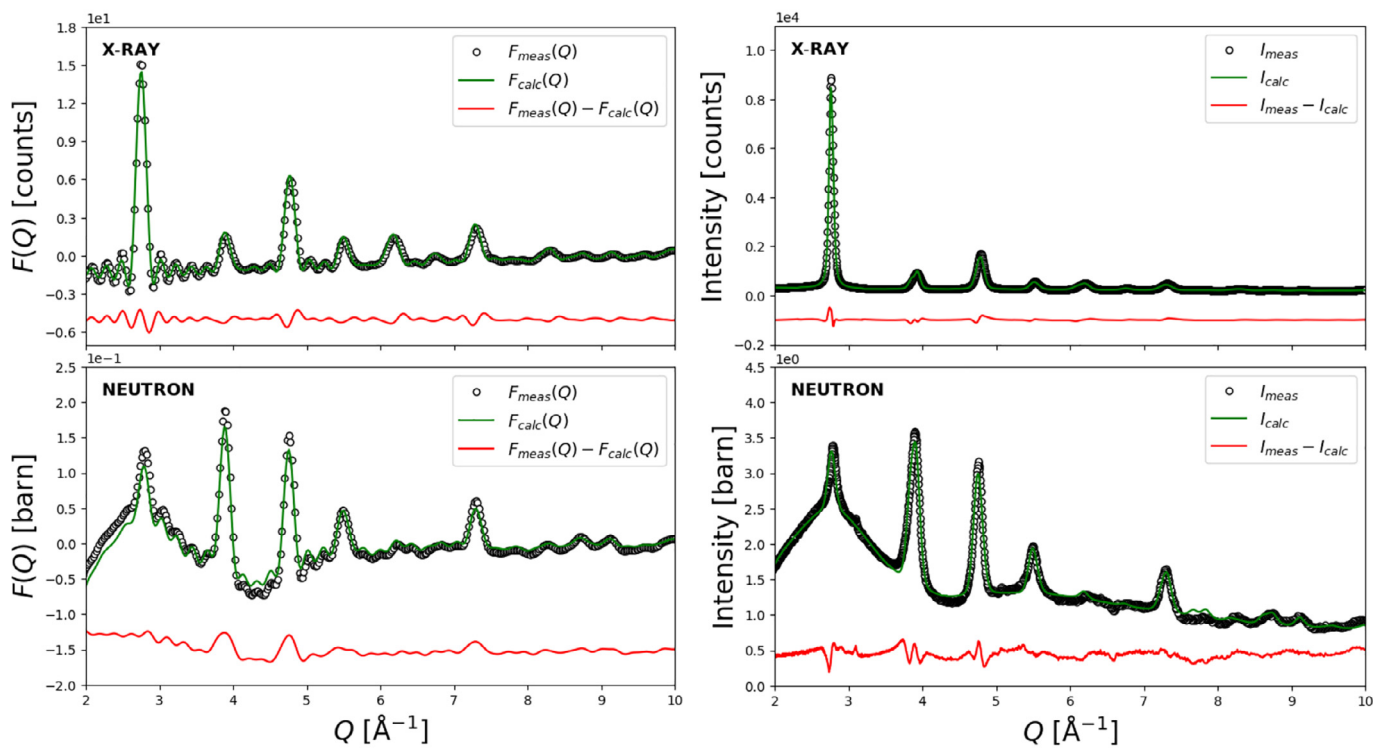| Atom | Site | $x$ | $y$ | $z$ | $U_{iso}$ | Occupancy |
|---|---|---|---|---|---|---|
| $M$ | 4a | 0 | 0 | 0 | 0.00471(7) | 1.0 |
| D | 8c | 1/4 | 1/4 | 1/4 | 0.1456(6) | 1.006(3) |
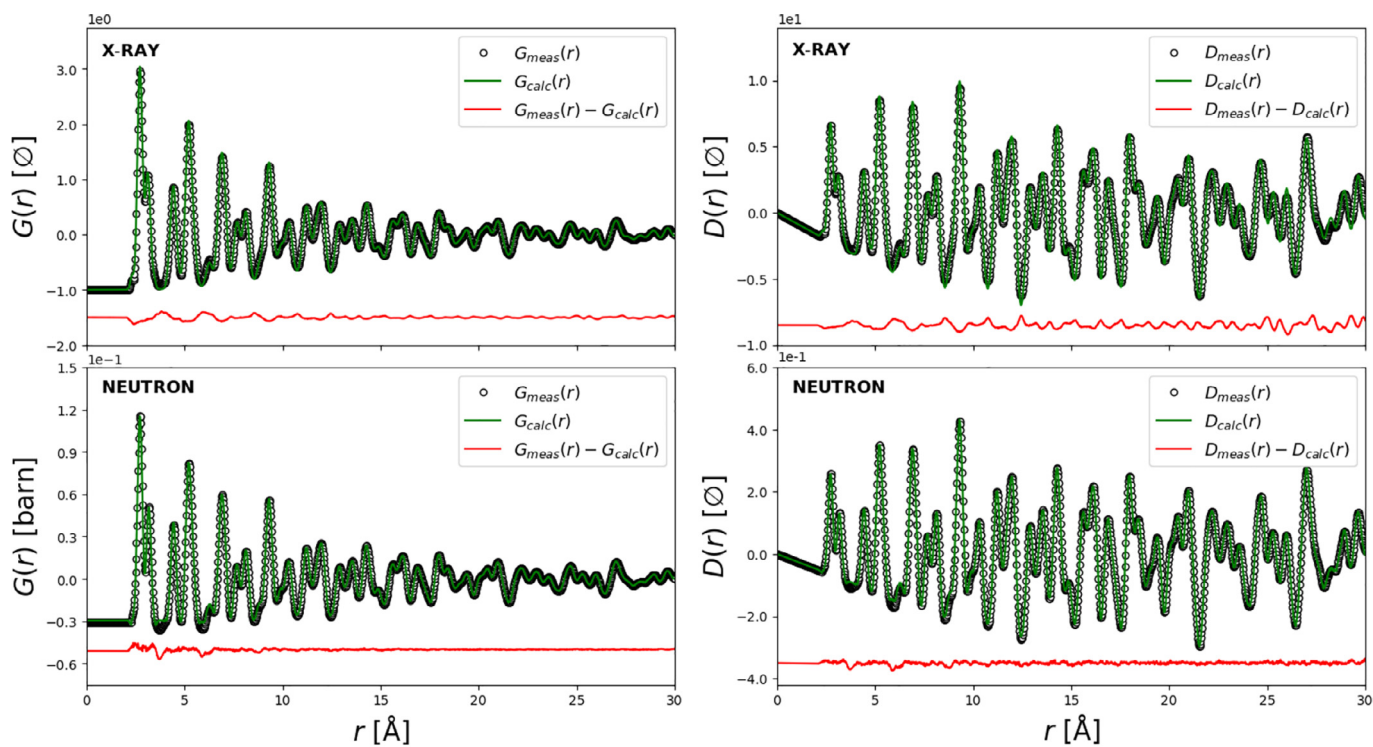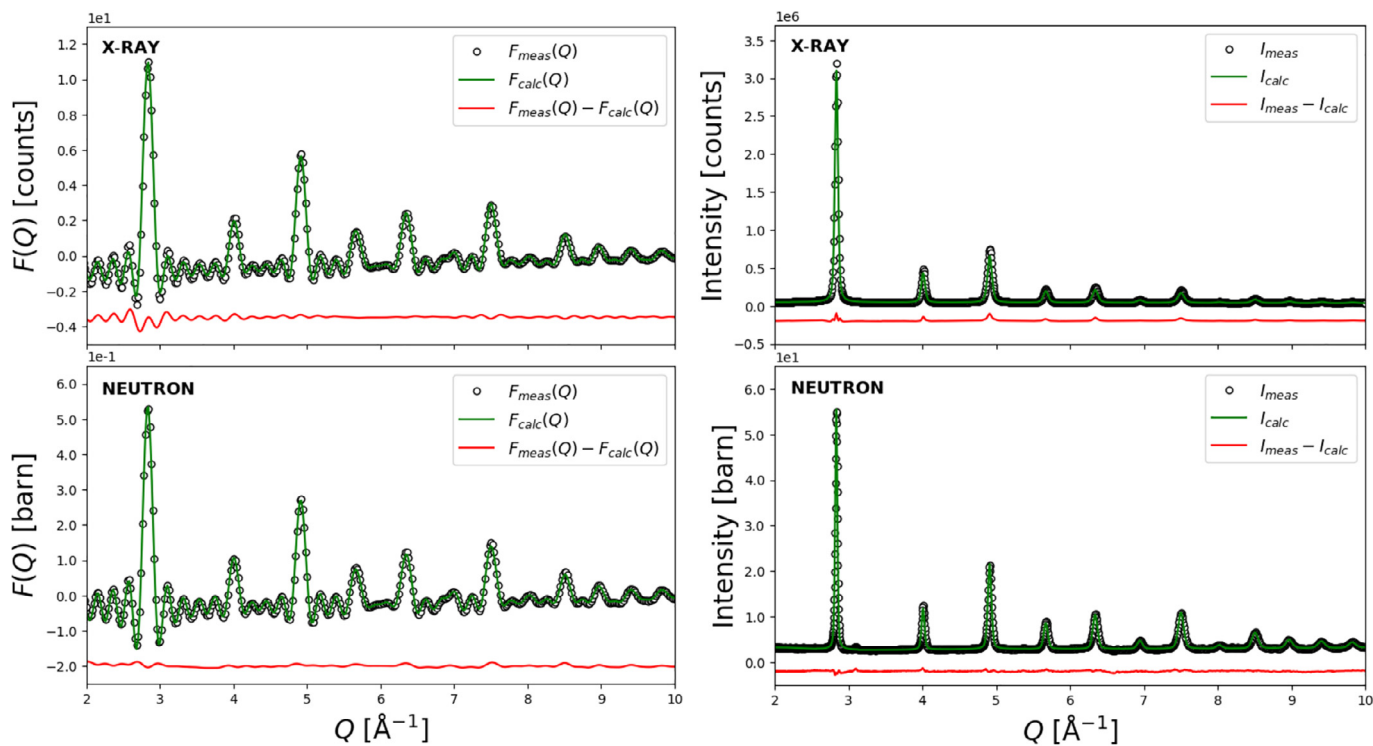
**Fig. 3.** RMC fits to the X-ray and neutron total scattering functions (a) $G(r)$, (b) $D(r)$, (c) $F(Q)$, and (d) Bragg scattering of TiVCrNb.

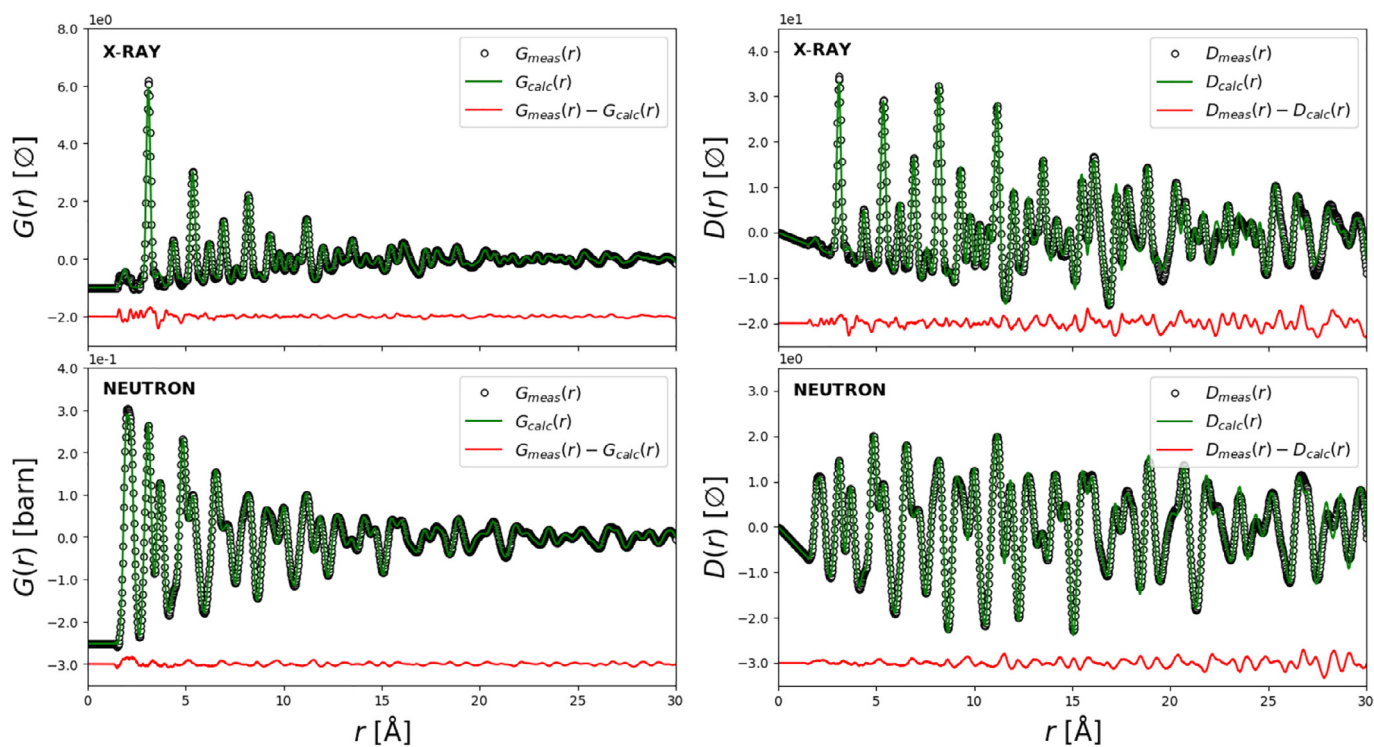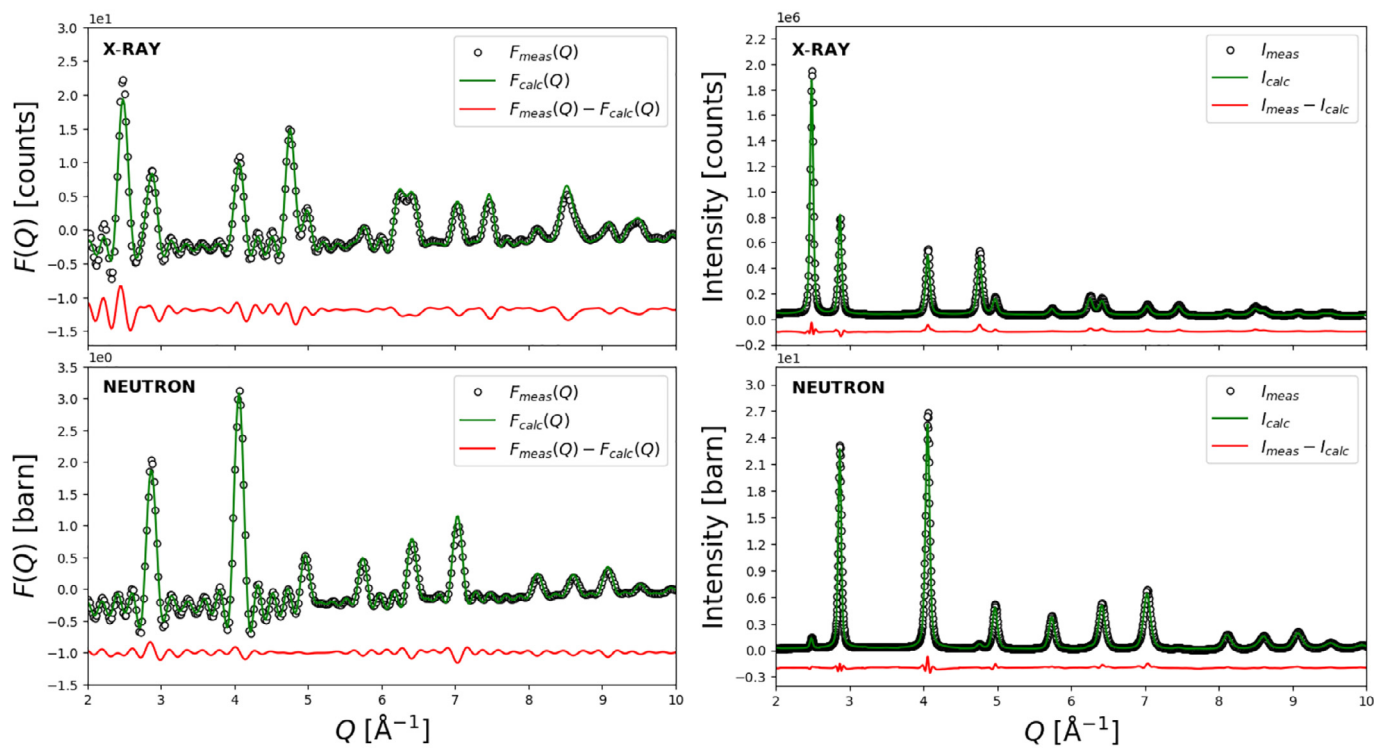**Fig. 4.** RMC fits to the X-ray and neutron total scattering functions (a) $G(r)$, (b) $D(r)$, (c) $F(Q)$, and (d) Bragg scattering of TiVCrNbD$_{2.2}$.
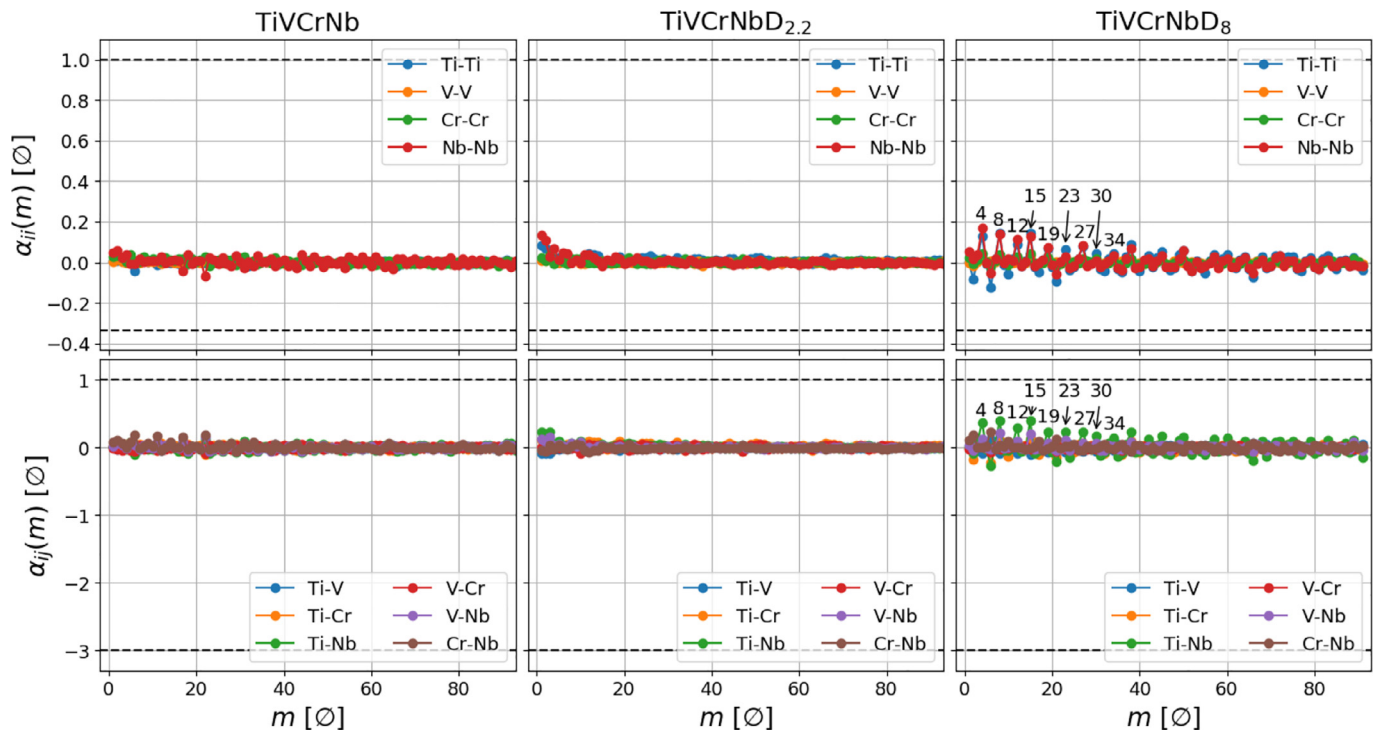
**(a)** $G(r)$



**(b)** $D(r)$



**(c)** $F(Q)$



**(d)** Bragg

**Fig. 5.** RMC fits to the X-ray and neutron total scattering functions (a) $G(r)$, (b) $D(r)$, (c) $F(Q)$, and (d) Bragg scattering of TiVCrNbD$_8$.

**Fig. 6.** Pairwise multicomponent short-range order parameters (PM-SRO) for the considered compositions extracted from the RMC large box models. The limiting values discussed in the text are indicated by dashed lines. The coordination shells where SRO is observed in TiVCrNbD$_8$ are marked with numbers.

**Table 2**

Nearest-neighbour distances measured in Å for the different atoms in TiVCrNbD$_{2.2}$.

| | | | Octahedral | | Tetrahedral | |
|---|---|---|---|---|---|---|
| | | $M_{2a}$ | $D_{2b}$ | $D_{4c}$ | $D_{4d}$ | $D_{8j}$ |
| | $M_{2a}$ | 2.80 | 1.64 | 1.60 | 1.80 | 1.77 |
| Octahedral | $D_{2b}$ | – | 2.80 | 1.60 | 1.80 | 0.68 |
| | $D_{4c}$ | – | – | 1.64 | 0.82 | 0.92 |
| Tetrahedral | $D_{4d}$ | – | – | – | 1.64 | 1.23 |
| | $D_{8j}$ | – | – | – | – | 0.96 |

in Table 2. We expect that neighbouring sites are unoccupied from the *Switendick criterion* [46], otherwise the D atoms would have been closer than 2 Å apart, and the criterion would be violated. Thus, it is ensured that all D atoms were further apart than 2.0 Å in the initial configurations of the RMC modelling.

Figs. 3–5 presents the obtained RMC fits to $G(r)$, $D(r)$, $F(Q)$ and the Bragg peak intensities for the as cast alloy, partially deuterated and fully deuterated compounds, respectively. The figures show that the obtained fits are in excellent agreement with the experimental data. The quality of the fits and the obtained models were comparable over the 10 RMC runs that were performed. The amount of disorder in the system can be characterized by calculating the pairwise multicomponent short-range order parameters (PM-SRO) from the RMC models [47]. These are defined as

$$\alpha_{ij}(m) = \frac{p_{ij}(m) - c_j}{\delta_{ij} - c_j} \tag{5}$$

where $c_j$ is the fraction of element $j$ in the alloy and $\delta_{ij} = 1$ if $i = j$ and $\delta_{ij} = 0$ otherwise. For an equiatomic HEA with $N = 4$ distinct chemical species $c_j = c = 1/4$. $p_{ij}(m)$ is the probability that an atom is of type $j$ in the $m$th coordination shell around a central atom of type $i$. It follows from the definition that $\sum_{j=1}^{4} p_{ij}(m) = 1$ for all elements $i$. The PM-SRO parameters can be understood as
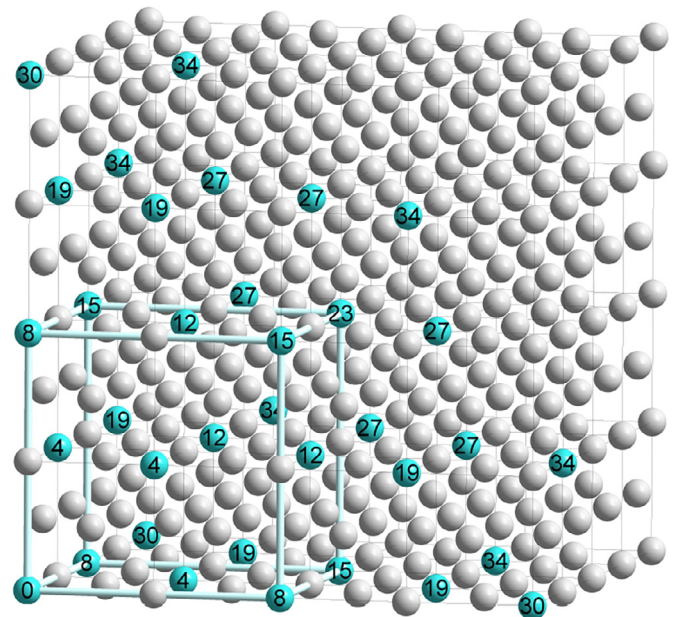


**Fig. 7.** A supercell made of $4 \times 4 \times 4$ face-centred cubic unit cells. The coordination numbers relative to the atom marked "0" in the bottom left corner are displayed on the cyan atoms. These atoms are located in coordination shells where there is increased probability of finding Ti around a Ti atom or Nb around a Nb atom in the RMC structure model of TiVCrNbD$_8$, i.e., coordination shell 4, 8, 12, 15, 19, 23, 27, 30 and 34. It can be seen that these sites form a $2 \times 2 \times 2$ supercell. One such supercell is outlined with thicker, cyan lines.

the relative deviation from a completely randomized solid solution. In the limiting scenarios, $\alpha_{ii}(m) = 1$ is obtained if there are only atoms of type $i$ and $\alpha_{ii}(m) = -1/3$ if there are no atoms of type $i$ in the $m$th coordination shell. A completely randomized solid solution without any SRO is characterized by $\alpha_{ij}(m) = 0$. For $i \neq j$,
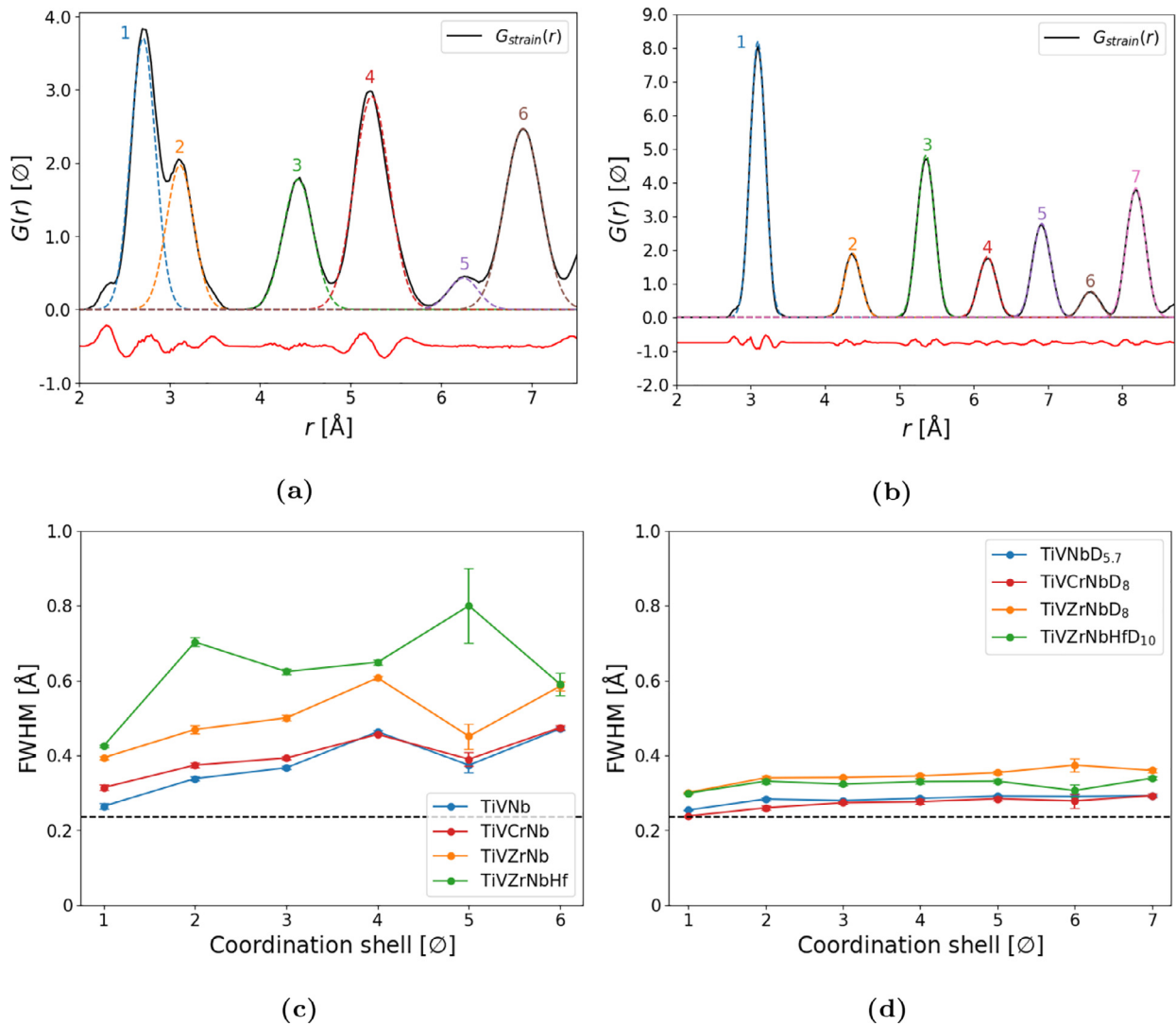
**Fig. 8.** Gaussian peaks fitted to the metal-only strain-PDF $G_{strain}(r)$ of TiVCrNb (a) and TiVCrNbD$_8$ (b). The peaks full-widths at half maximum (FWHM) are compared to values from a similar analysis for TiVNb, TiVZrNb and TiVZrNbHf (c) and the corresponding dideuterides (d). Values for these other systems are adopted from Ref. [48]. In (c) and (d), the dashed black lines indicates the typical magnitude of the FWHM corresponding to thermal vibrations. Assuming a normal distribution of oscillations and a typical mean-square displacement ($msd$ or $U_{iso}$) of 0.01 Å, a value of around 0.24 Å is obtained using the relation FWHM $= 2\sqrt{2\ln(2) \cdot msd}$.

$\alpha_{ij}(m) = -3$ if there are only atoms of type $j$ in the coordination shell and $\alpha_{ij}(m) = 1$ if there are no atoms of type $j$. The PM-SRO parameters of the obtained RMC models are shown in Fig. 6. In general, the elements seems to be well dispersed and the metal lattice can be characterized as being very close to a random solid solution. However, there are some tendencies towards ordering in the deuterides. In particular, there is an increased probability for Nb to be coordinated by itself in the first coordination spheres of TiVCrNbD$_{2.2}$. TiVCrNbD$_8$ has the same local ordering as reported for TiVNbD$_{5.7}$ [48]. In particular, the probability is higher for Ti and Nb to be coordinated by itself in the 4th, 8th, 12th, 15th, 19th, 23rd, 27th and 30th coordination sphere. These coordination spheres corresponds to a $2 \times 2 \times 2$ face-centred cubic supercell, as presented in Fig. 7. Nevertheless, the deviations from a completely randomized solid solution are far from the limiting scenarios outlined above.

Many exceptional properties reported for HEAs have been attributed to severe lattice distortion caused by differently sized

atoms in the alloy [13]. The lattice distortion is often quantified by the relative variation in atom sizes $\delta r$ that is defined as

$$\delta r = \sqrt{\sum_{i=1}^{N} c_i \left(1 - \frac{r_i}{\bar{r}}\right)^2} \cdot 100\% \qquad (6)$$

where $\bar{r} = \sum_{i=1}^{N} c_i r_i$ with $\{c_i\}_{i=1}^{N}$ and $\{r_i\}_{i=1}^{N}$ as the concentrations and radii of the $N$ elements in the HEA, respectively. The direct evidence of this effect is limited in the literature [49]. One reason behind this is the difficulty to perform suitable measurements. It has been suggested that the level of local lattice strain can be assessed from analyzing the full-widths at half maximum (FWHM) of the peaks in a *strain-PDF* obtained from RMC modelling [50]. Such an analysis has recently been performed for TiVNb ($\delta r = 4.29\%$), TiVZrNb ($\delta r = 6.87\%$) and TiVZrNbHf ($\delta r = 6.96\%$) and the corresponding dideuterides [48]. For these systems it was observed that the FWHM of the peaks in the strain-PDF of the alloys increased
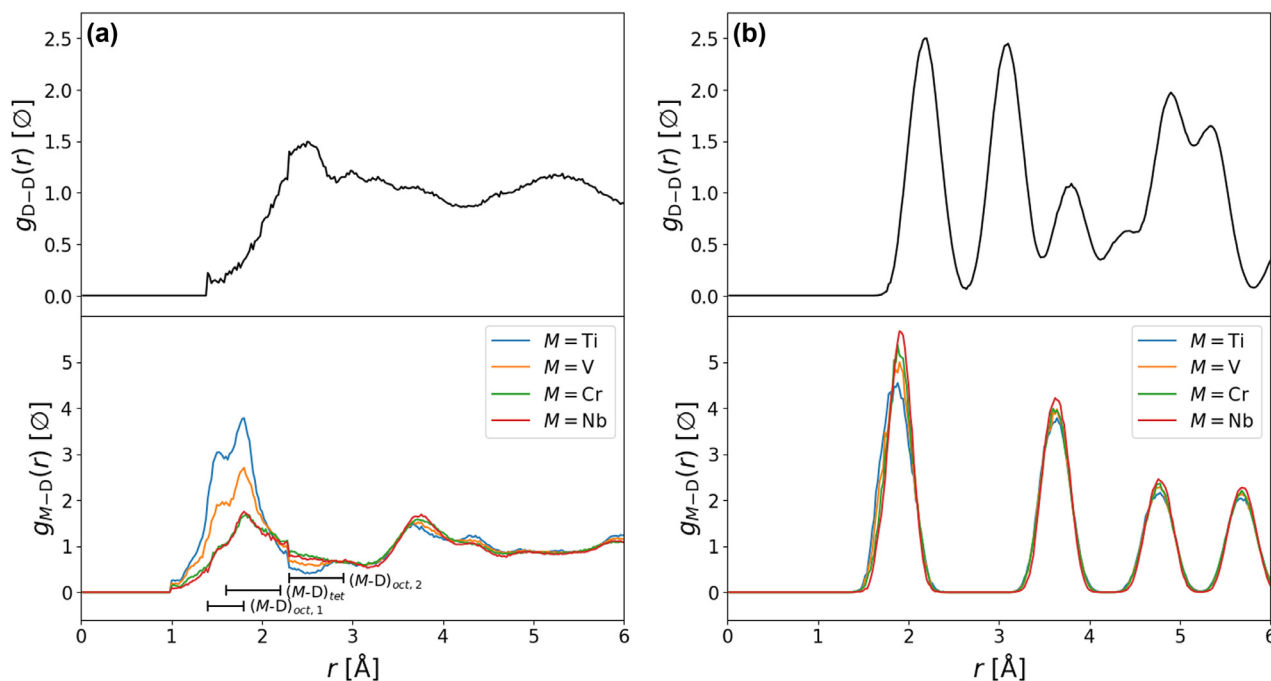
**Fig. 9.** The D-D and *M*-D partial PDFs for TiVCrNbD$_{2.2}$ (a) and TiVCrNbD$_8$ (b) averaged over the ten fits obtained from the RMC modelling. The horizontal black lines indicates one standard deviation about the mean *M*−D nearest-neighbour and second-nearest neighbour distances for the tetrahedral and octahedral interstices in the RMC model of TiVCrNbD$_{2.2}$.

significantly from TiVNb to TiVZrNb and TiVZrNbHf. This is expected from the higher $\delta r$ values in the latter HEAs. The strain was lower in the corresponding deuterides, but the trend was still present. The atomic radii of Ti, V, Cr and Nb are 1.46 Å, 1.32 Å, 1.25 Å and 1.43 Å, respectively [13]. Thus, TiVCrNb has $\delta r = 6.18\%$, and it should be expected that also this alloy is severely strained. However, Fig. 8 demonstrates that the strain is comparable with that obtained for TiVNb for which most of the FWHM can be explained by thermal vibrations. The main difference between these alloys is whether the element that causes $\delta r$ to increase is smaller or larger than the others. Thus, our analysis indicates that the HEA lattice is less prone towards strain when smaller elements are introduced into a matrix of larger atoms. Since $\delta r$ is insensitive to this, it can be a misleading measure of the local lattice distortion in a HEA.

Fig. 9 presents the D-D and *M*-D partial PDFs for TiVCrNbD$_{2.2}$ and TiVCrNbD$_8$. The first peak in the D-D partial is in both cases just above 2 Å in compliance with the Switendick criterion. This result comes solely from the experimental data and not from any imposed constraint or penalty during the modelling process. The *M*-D partials of TiVCrNbD$_8$ are characterized by well-defined coordination shells. However, for TiVCrNbD$_{2.2}$ the *M*-D partials have a continuous distribution. Moreover, for this compound it is observed that D has a significantly higher probability of being coordinated by Ti and V than Cr and Nb. This result is in compliance with results reported for deuterides formed from Ti$_{0.45}$Cr$_{0.35}$Mo$_{0.20}$ [24]. Moreover, it is also clear that this effect is only present in the first coordination sphere ($r < 2.2$ Å). The first two peaks in the *M*-D partials are attributed to the octahedral and tetrahedral interstices, respectively. In the tetrahedral interstices, D is coordinated by four

nearest-neighbour metals at $r = 1.9(3)$ Å in the RMC model. In the octahedral interstices, the metal octahedron surrounding D is made out of two nearest-neighbour and four second-nearest neighbour metals. The distance from D to these are $r = 1.6(2)$ Å and $r = 2.6(3)$ Å, respectively. The mean values of the octahedral and tetrahedral nearest-nighbour distances are in very good agreement with the values expected from crystallography (see Table 2). Analyses of the local coordination environments indicates that the octahedral second-nearest neighbours are randomly distributed. Fig. 10 shows the fraction of occupied tetrahedral and octahedral interstices in the RMC structure model with different metals as nearest neighbours. It is clear that a larger fraction of the sites are occupied if the *VEC* of the nearest-neighbours are lower. Thus, the destabilization effect presented in Ref. [21] is also present at the local level. This suggests that it could be possible to increase the reversible hydrogen storage capacity by fine-tuning the HEA composition. In this endeavor it should be kept in mind that *VEC* > 5.0 often results in a reduction in the maximum hydrogen storage capacity [21]. Thus, the overall *VEC* should be kept at 5.0. One possibility to achieve this is to reduce the amount of Ti and Cr equally. Another strategy is to reduce the amount of Ti and add an appropriate amount of another element with higher *VEC*, e.g. Mn, Fe or Ni.

The analyses presented above indicate that the remaining hydrogen atoms in the partially desorbed material occupy sites with all possible combinations of nearest neighbours in both octahedral and tetrahedral interstices. Thus, the local metallic environments around the hydrogen atoms are very diverse. This should also be reflected in the vibrational density of states (vDOS) of the hydrogen atoms as measured by INS. Fig. 11 presents the measured INS
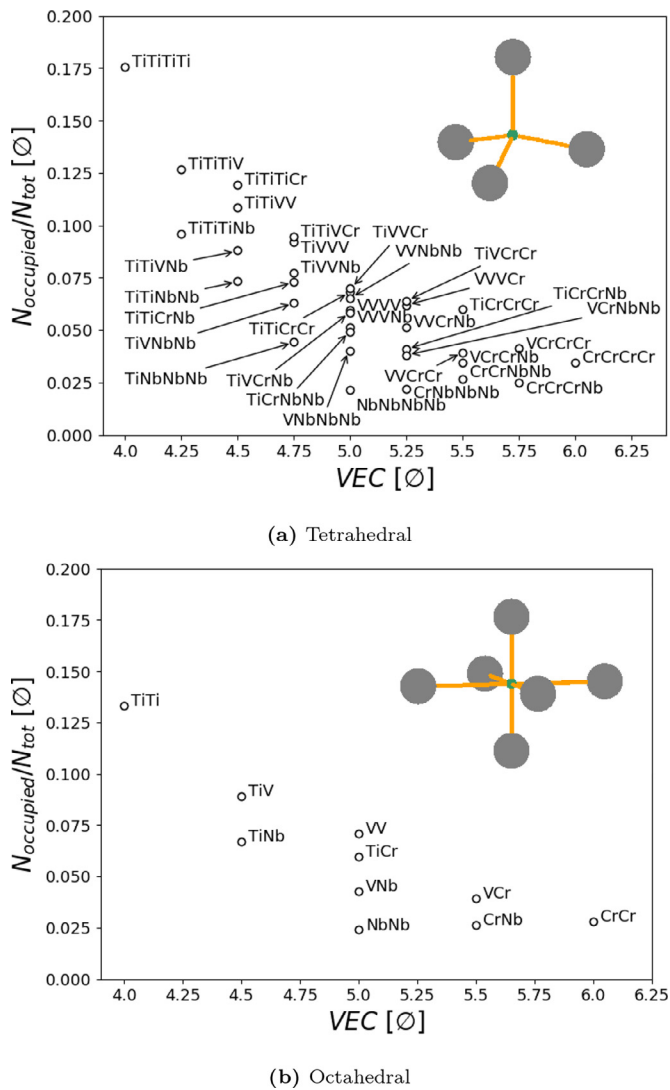
**(a)** Tetrahedral



**(b)** Octahedral

**Fig. 10.** The fraction of tetrahedral and octahedral interstices with different nearest-neighbour metals that are occupied by D within the RMC structure model of $TiVCrNbD_{2.2}$. The insets presents the polyhedra with the D and $M$ indicated by green and grey balls, respectively. For the octahedron, the second-nearest metals are within the horizontal plane. (For interpretation of the references to colour in this figure legend, the reader is referred to the web version of this article.)

spectra of TiVCrNb, $TiVCrNbH_{2.4}$ and $TiVCrNbH_8$ as well as the total scattering contributions calculated from DFT for the hydrides. In the INS spectrum of $TiVCrNbH_8$ there is a single, broad vibrational band in the range 150–300 meV. The energy range of the vibration is in compliance with that expected for a regular tetrahedral environment [51].

The INS spectra can be evaluated with respect to the models obtained from the RMC structure modelling. Fig. 9 shows that the $M$–D bond length distribution is separated into well-defined peaks in the RMC structure model of $TiVCrNbD_8$. The distribution and disorder of $M$–D bonding in $TiVCrNbD_8$ is manifested in the widths of these peaks. Due to the disordered atomic arrangement with several differently sized atoms, it should be expected that the INS spectra and vDOS reflect the diversity in different $M$–H bond lengths. Indeed, the broadness of the vibrational band is much larger than expected for a binary metal hydride. Thus, the INS spectrum of $TiVCrNbH_8$ represents a large diversity for the $M$–

H bonds and hydrogen vibrations. It should be noted that no intensity is observed in the energy range around 128 meV where vibrations from hydrogen in an octahedral environment is expected [51]. This indicates that hydrogen solely occupies the tetrahedral interstices in $TiVCrNbH_8$. Furthermore, DFT calculations substantiate these findings. Fig. 11 also displays the *in silico* INS spectrum of $TiVCrNbH_8$ where contributions from all the binary metal hydrides have been summed. The *in silico* INS spectra of the individual metal hydrides show some splitting of the peaks. However, when all the binary spectra are combined the broadness of the measured INS spectrum is well reproduced, once again indicating a large diversity in $M$–H bonds and hydrogen vibrations. The overall shape of the experimental and *in silico* spectra are in compliance, but the vibrational energies are slightly overestimated in the latter. However, this is a common trait when calculating phonon spectra by DFT where the harmonic nature is often exaggerated [52–55].

Fig. 11 also presents the INS spectrum of $TiVCrNbH_{2.4}$. In this case, the INS spectrum is smeared and without sharp features with two very broad bands centred at 90 meV and 170 meV. This is in contrast to the well-defined peak in the measured INS spectrum of $TiVCrNbH_8$. Yet, the spectrum is in contrast to that measured of the hydrogen-free alloy which is nought above the metal phonons at 0–70 meV confirming the presence of hydrogen in $TiVCrNbH_{2.4}$. Fig. 9 shows that the $M$–D bond length distribution in $TiVCrNbD_{2.2}$ is continuous. This is a very different characteristic than the well-defined peaks in the corresponding distribution of $TiVCrNbD_8$. This observation provides an indication of the severity of the disorder in the hydrogen sublattice of $TiVCrNbH_{2.4}$. It seems reasonable that a continuous distribution of $M$–H bond lengths in $TiVCrNbH_{2.4}$ could cause a continuous vDOS for hydrogen with a corresponding, continuous INS spectrum like the one presented in Fig. 11. Thus, the RMC structure model provides a possible explanation to the smeared INS spectrum of $TiVCrNbH_{2.4}$. The *in silico* spectrum presented in Fig. 11 is generated from a $2 \times 2 \times 2$ supercell with nominal composition $TiVCrNbH_{2.25}$ by the random structure approach. The spectrum displays a wide range of distinct hydrogen modes from the different local environments for hydrogen in the supercell. However, because of the limited size of the model, only a limited number of vibrational modes are observed. The model is, therefore, not able to reproduce the continuous shape of the experimental INS spectrum. We expect that a larger supercell would provide a more realistic vDOS, but calculations from such a model would be computationally expensive and is, for this reason, not pursued. Thus, it is concluded that the calculation reproduces the most important aspects of the spectra, i.e., the diversity of local environments for hydrogen. As mentioned above, the phonon calculation overestimates the vibrational energies, and with this in mind, also the low energy vibrational modes for hydrogen is accounted for.

Fig. 12 shows the distribution of deuterium atoms in the RMC structure models of $TiVCrNbD_{2.2}$ and $TiVCrNbD_8$ projected onto the *xy*-, *xz*- and *yz*-plane of the respective unit cells. The figure clearly demonstrates that the probability of finding a deuterium atom outside the tetrahedral interstices in $TiVCrNbD_8$ is zero. For $TiVCrNbD_{2.2}$ the probability of finding the deuterium atoms in the crystallographically expected positions is high. However, in this case there is also a significant probability of observing the deuterium atoms between the octahedral and tetrahedral interstices. This indicate that hydrogen atoms are mobile between the available sites. Quasi-elastic neutron scattering (QENS) could reveal if the diffusion is predominately local or long-range, but this is beyond the scope of this work and thus left for future studies.
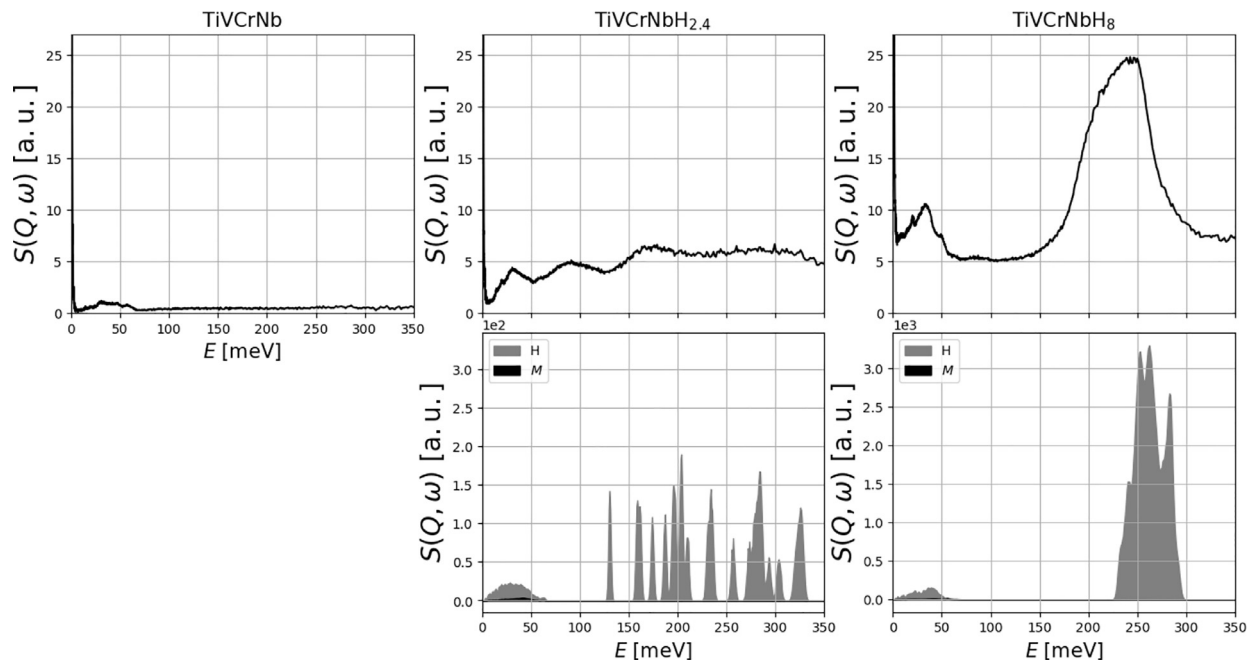
**Fig. 11.** Measured INS spectra (top row) and *in silico* equivalents calculated by DFT (bottom row). The *in silico* spectrum compared to TiVCrNbH$_{2.4}$ is generated from a $2 \times 2 \times 2$ supercell with nominal composition TiVCrNbH$_{2.25}$. The *in silico* spectrum compared to TiVCrNbH$_8$ is the sum of those calculated for the binary dihydrides.
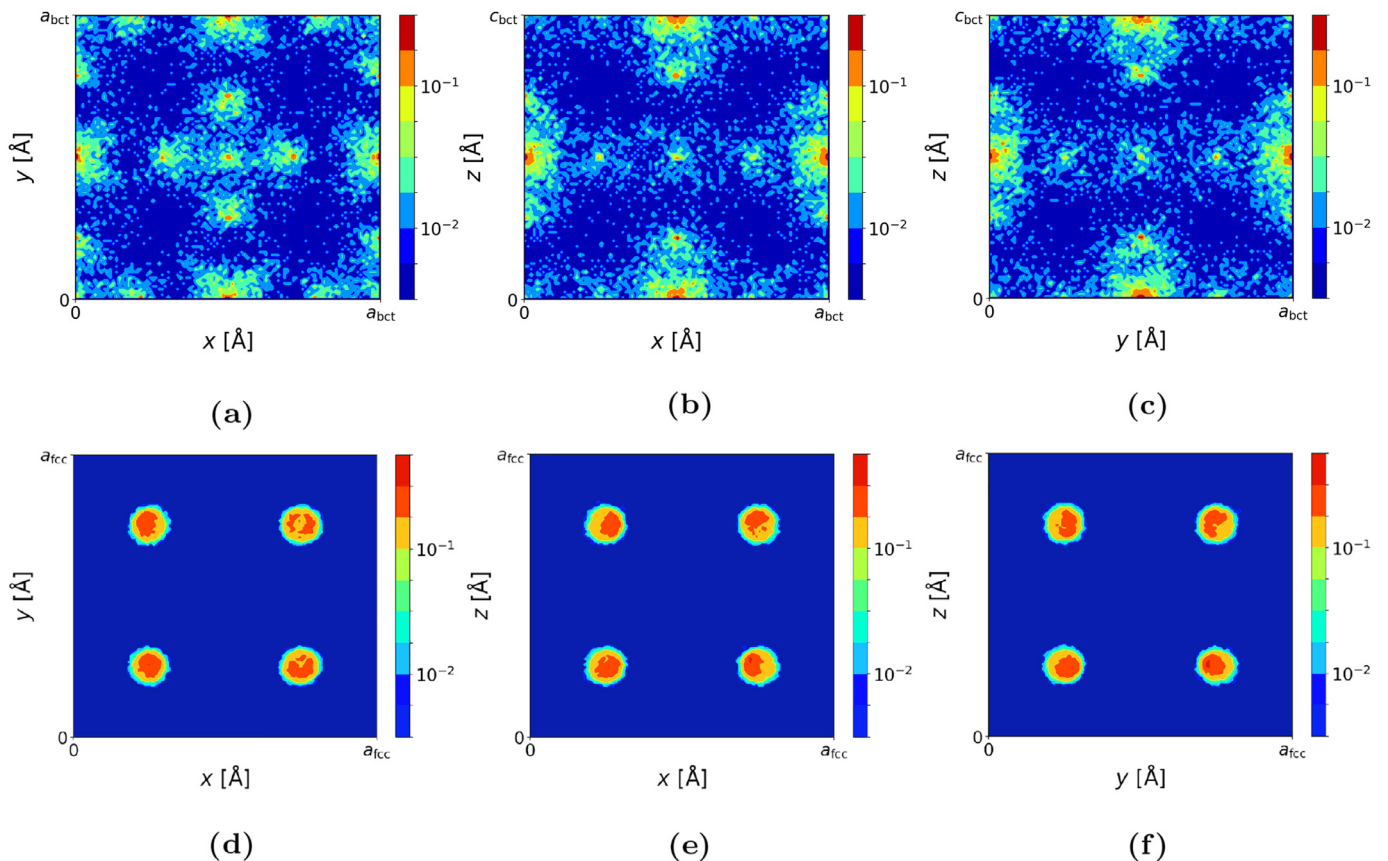


**Fig. 12.** The distribution of D in the RMC structure model of TiVCrNbD$_{2.2}$ (bct structure) projected onto the *xy*- (a), *xz*- (b) and *yz*-plane of the unit cell. The same is shown for TiVCrNbD$_8$ (CaF$_2$-type structure) in (d), (e) and (f). The colorbars indicates the percentage of D at any position in the unit cells.

## 4. Conclusions

The present work has explored the average and local structure of TiVCrNbD$_x$, $x = 0, 2.2, 8.0$ using total scattering measurements and RMC structure modelling. The metal lattices are close to random solid solutions in the obtained models. TiVCrNb is a bcc ($Im\bar{3}m$) HEA with $\delta r = 6.18\%$. The prevailing opinion in the literature of HEAs is that a larger $\delta r$ indicates a more severely distorted lattice. However, this work demonstrates that the amount of local lattice strain in TiVCrNb as measured by the strain-PDF

obtained from the RMC structure model is comparable to that of TiVNb ($Im\bar{3}m$) with $\delta r = 4.29\%$. This demonstrates that $\delta r$ can be a misleading measure of the local lattice strain in a HEA.

PCIs shows that the structure changes from TiVCrNbD$_{2.2}$ to TiVCrNbD$_8$ in a single step phase transition. TiVCrNbD$_8$ adopts a CaF$_2$-type structure ($Fm\bar{3}m$) in which the deuterium atoms solely occupy the tetrahedral interstices. INS and DFT calculations provide complementary evidence of this. The RMC structure model reveals a tendency for Ti and Nb short-range order where these metals form $2 \times 2 \times 2$ face-centred cubic supercells. TiVCrNbD$_{2.2}$ adopts a bct ($I4/mmm$) structure where the deuterium atoms occupy both tetrahedral and octahedral interstices with low occupancies. The $M$–D bond length distribution is continuous in the RMC structure model of this compound. This suggests that also the hydrogen vDOS could be continuous as observed in the measured INS spectrum of TiVCrNbH$_{2.4}$. Moreover, in the RMC structure model of TiVCrNbD$_{2.2}$ there is a significantly higher portion of occupied sites where the nearest-neighbour metals have lower $VEC$. The effect is present for both tetrahedral and octahedral interstices. This observation indicates that the reversible hydrogen storage capacity could be increased from 1.96 wt.% H in similar compounds if the composition is finely tuned. This should be done in such a way that the overall $VEC$ is kept constant at $VEC = 5.0$ to avoid reduction in the reversible hydrogen storage capacity.

## Declaration of Competing Interest

The authors declare that they have no known competing financial interests or personal relationships that could have appeared to influence the work reported in this paper.

## Acknowledgements

## References

[1] M. Hirscher, V.A. Yartys, M. Baricco, J.B. von Colbe, D. Blanchard, R.C. Bowman Jr., D.P. Broom, C.E. Buckley, F. Chang, P. Chen, Y.W. Cho, J.-C. Crivello, F. Cuevas, W.I.F. David, P.E. de Jong, R.V. Denys, M. Dornheim, M. Felderhoff, Y. Filinchuk, G.E. Froudakis, D.M. Grant, E.M. Gray, B.C. Hauback, T. He, T.D. Humphries, T.R. Jensen, S. Kim, Y. Kojima, M. Latroche, H.-W. Li, M.V. Lototskyy, J.W. Makepeace, K.T. Møller, L. Naheed, P. Ngene, D. Noréus, M.M. Nygård, S.-i. Orimo, M. Paskevicius, L. Pasquini, D.B. Ravnsbæk, M.V. Sofianos, T.J. Udovic, T. Vegge, G.S. Walker, C.J. Webb, C. Weidenthaler, C. Zlotea, Materials for hydrogen-based energy storage – past, recent progress and future outlook, J. Alloys Compd. 827 (2020) 153548.

[2] M. Paskevicius, L.H. Jepsen, P. Schouwink, R. Černý, D.B. Ravnsbæk, Y. Filinchuk, M. Dornheim, F. Besenbacher, T.R. Jensen, Metal borohydrides and derivatives–synthesis, structure and properties, Chem. Soc. Rev. 46 (5) (2017) 1565–1634.

[3] C. Frommen, M. Sørby, M. Heere, T. Humphries, J. Olsen, B. Hauback, Rare earth borohydrides-crystal structures and thermal properties, Energies 10 (12) (2017) 2115.

[4] C. Milanese, T.R. Jensen, B.C. Hauback, C. Pistidda, M. Dornheim, H. Yang, L. Lombardo, A. Züttel, Y. Filinchuk, P. Ngene, P.E. de Jongh, C.E. Buckley, E.M. Dematteis, M. Baricco, Complex hydrides for energy storage, Int. J. Hydrog. Energy 44 (15) (2019) 7860–7874.

[5] V.A. Yartys, M.V. Lototskyy, E. Akiba, R. Albert, V.E. Antonov, J.R. Ares, M. Baricco, N. Bourgeois, C.E. Buckley, J.M. Bellosta von Colbe, J.-C. Crivello, F. Cuevas, R.V. Denys, M. Dornheim, M. Felderhoff, D.M. Grant, B.C. Hauback, T.D. Humphries, I. Jacob, T.R. Jensen, P.E. de Jongh, J.-M. Joubert, M.A. Kuzovnikov, M. Latroche, M. Paskevicius, L. Pasquini, L. Popilevsky, V.M. Skripnyuk, E. Rabkin, M.V. Sofianos, A. Stuart, G. Walker, H. Wang, C.J. Webb, M. Zhu, Magnesium based materials for hydrogen based energy storage: Past, present and future, Int. J. Hydrog. Energy 44 (15) (2019) 7809–7859.

[6] R. Cohen, K. West, J. Wernick, Degradation of LaNi5 by temperature-induced cycling, J. Less Common Metals 73 (2) (1980) 273–279.

[7] L. Schlapbach, T. Riesterer, The activation of FeTi for hydrogen absorption, Appl. Phys. A 32 (4) (1983) 169–182.

[8] J. Joubert, M. Latroche, A. Percheron-Guégan, Hydrogen absorption properties of several intermetallic compounds of the ZrNi system, J. Alloys Compd. 231 (1-2) (1995) 494–497.

[9] G. Walker, Solid-State Hydrogen Storage: Materials and Chemistry, Elsevier, 2008.

[10] H. Chung, J.-Y. Lee, Effect of partial substitution of Mn and Ni for Fe in FeTi on hydriding kinetics, Int. J. Hydrog. Energy 11 (5) (1986) 335–339.

[11] S.W. Lambert, D. Chandra, W.N. Cathey, F.E. Lynch, R.C. Bowman Jr., Investigation of hydriding properties of LaNi4.8Sn0.2, LaNi4.27Sn0.24 and La0.9Gd0.1Ni5 after thermal cycling and aging, J. Alloys Compd. 187 (1) (1992) 113–135.

[12] B.-H. Liu, D.-M. Kim, K.-Y. Lee, J.-Y. Lee, Hydrogen storage properties of TiMn2-based alloys, J. Alloys Compd. 240 (1-2) (1996) 214–218.

[13] D. Miracle, O. Senkov, A critical review of high entropy alloys and related concepts, Acta Mater. 122 (2017) 448–511.

[14] M. Sahlberg, D. Karlsson, C. Zlotea, U. Jansson, Superior hydrogen storage in high entropy alloys, Sci. Rep. 6 (2016) 36770.

[15] D. Karlsson, G. Ek, J. Cedervall, C. Zlotea, K.T. Møller, T.C. Hansen, J. Bednarcik, M. Paskevicius, M.H. Sørby, T.R. Jensen, U. Jansson, M. Sahlberg, Structure and hydrogenation properties of a HfNbTiVZr high-entropy alloy, Inorg. Chem. 57 (4) (2018) 2103–2110.

[16] C. Zlotea, M. Sow, G. Ek, J.-P. Couzinié, L. Perrière, I. Guillot, J. Bourgon, K. Møller, T. Jensen, E. Akiba, M. Sahlberg, Hydrogen sorption in TiZrNbHfTa high entropy alloy, J. Alloys Compd. 775 (2018) 667–674.

[17] M.M. Nygård, G. Ek, D. Karlsson, M. Sahlberg, M.H. Sørby, B.C. Hauback, Hydrogen storage in high-entropy alloys with varying degree of local lattice strain, Int. J. Hydrog. Energy 44 (55) (2019) 29140–29149.

[18] J. Montero, C. Zlotea, G. Ek, J.-C. Crivello, L. Laversenne, M. Sahlberg, TiVZrNb multi-principal-element alloy: Synthesis optimization, structural, and hydrogen sorption properties, Molecules 24 (15) (2019) 2799.

[19] H. Shen, J. Hu, P. Li, G. Huang, J. Zhang, J. Zhang, Y. Mao, H. Xiao, X. Zhou, X. Zu, X. Long, S. Peng, Compositional dependence of hydrogenation performance of Ti-Zr-Hf-Mo-Nb high-entropy alloys for hydrogen/tritium storage, J. Mater. Sci. Technol. 55 (2020) 116–125.

[20] M.O. de Marco, Y. Li, H.-W. Li, K. Edalati, R. Floriano, Mechanical synthesis and hydrogen storage characterization of MgVCr and MgVTiCrFe high-entropy alloy, Adv. Eng. Mater. 22 (2) (2019) 1901079.

[21] M.M. Nygård, G. Ek, D. Karlsson, M.H. Sørby, M. Sahlberg, B.C. Hauback, Counting electrons – a new approach to tailor the hydrogen sorption properties of high-entropy alloys, Acta Mater. 175 (2019) 121–129.

[22] P. Edalati, R. Floriano, A. Mohammadi, Y. Li, G. Zepon, H.-W. Li, K. Edalati, Reversible room temperature hydrogen storage in high-entropy alloy TiZrCrMnFeNi, Scr. Mater. 178 (2020) 387–390.

[23] R. McGreevy, L. Pusztai, Reverse Monte Carlo simulation: a new technique for the determination of disordered structures, Mol. Simul. 1 (6) (1988) 359–367.

[24] K. Iwase, T. Kamiyama, Y. Nakamura, K. Mori, M. Yonemura, S. Harjo, T. Ishigaki, E. Akiba, Average and local structures in hydrogen absorbing Ti–Cr–Mo alloy, Mater. Trans. 47 (2) (2006) 271–274.

[25] H. Brinks, A. Fossdal, R. Bowman, B. Hauback, Pressure–composition isotherms of TbNiAlHx, J. Alloys Compd. 417 (1) (2006) 92–95.

[26] T. Egami, S.J. Billinge, Underneath the Bragg peaks: structural analysis of complex materials, Pergamon, 2012.

[27] D.A. Keen, A comparison of various commonly used correlation functions for describing total scattering, J. Appl. Crystallogr. 34 (2) (2001) 172–177.

[28] T. Watanuki, A. Machida, T. Ikeda, A. Ohmura, H. Kaneko, K. Aoki, T. Sato, A. Tsai, Development of a single-crystal X-ray diffraction system for hydrostatic-pressure and low-temperature structural measurement and its application to the phase study of quasicrystals, Philos. Mag. 87 (18-21) (2007) 2905–2911.

[29] A.K. Soper, GudrunN and GudrunX: Programs for Correcting raw Neutron and X-ray Diffraction data to Differential Scattering Cross Section, Science & Technology Facilities Council Swindon, UK, 2011.

[30] A.C. Larson, R.B. Von Dreele, General structure analysis system (GSAS), Los Alamos Natl. Labor. Rep. LAUR 86-749 (1994).

[31] B.H. Toby, EXPGUI, a graphical user interface for GSAS, J. Appl. Crystallogr. 34 (2) (2001) 210–213.

[32] P. Thompson, D. Cox, J. Hastings, Rietveld refinement of Debye–Scherrer synchrotron X-ray data from Al2O3, J. Appl. Crystallogr. 20 (2) (1987) 79–83.

[33] S. Ikeda, J.M. Carpenter, Wide-energy-range, high-resolution measurements of neutron pulse shapes of polyethylene moderators, Nuclear Instrum. Methods Phys. Res. Sect. A 239 (3) (1985) 536–544.

[34] M.G. Tucker, D.A. Keen, M.T. Dove, A.L. Goodwin, Q. Hui, RMCProfile: reverse Monte Carlo for polycrystalline materials, J. Phys. 19 (33) (2007) 335218.

[35] R.S. Pinna, S. Rudić, S.F. Parker, J. Armstrong, M. Zanetti, G. Škoro, S.P. Waller, D. Zacek, C.A. Smith, M.J. Capstick, D.J. McPhail, D.E. Pooley, G.D. Howells, G. Gorini, F. Fernandez-Alonso, The neutron guide upgrade of the TOSCA spectrometer, Nuclear Instrum. Methods Phys. Res. Sect. A 896 (2018) 68–74.

[36] Ø. S. Fjellvåg, B.C. Hauback, J. Armstrong, M.M. Nygård, Mechanism of hydrogen residue in metal hydrides formed from high-entropy alloys by inelastic neutron spectroscopy, STFC ISIS Neutron and Muon Source (2019), doi:10.5286/ISIS.E.RB1920331.

[37] G. Kresse, J. Furthmüller, Self-interaction correction to density functional approximation for many electron systems, Phys. Rev. B 54 (1996a) 11169.

[38] G. Kresse, J. Furthmüller, Efficiency of ab-initio total energy calculations for metals and semiconductors using a plane-wave basis set, Comput. Mater. Sci. 6 (1) (1996b) 15–50.

[39] J.P. Perdew, K. Burke, M. Ernzerhof, Generalized gradient approximation made simple, Phys. Rev. Lett. 77 (18) (1996) 3865.

[40] A. Liechtenstein, V. Anisimov, J. Zaanen, Density-functional theory and strong interactions: Orbital ordering in Mott-Hubbard insulators, Phys. Rev. B 52 (8) (1995) R5467.

[41] S. Dudarev, G. Botton, S.Y. Savrasov, Z. Szotek, W. Temmerman, A. Sutton, Electronic structure and elastic properties of strongly correlated metal oxides from first principles: LSDA+ U, SIC-LSDA and EELS study of UO2 and NiO, Phys. Status Solidi A 166 (1) (1998) 429–443.

[42] A. Togo, F. Oba, I. Tanaka, First-principles calculations of the ferroelastic transition between rutile-type and $CaCl_2$-type $SiO_2$ at high pressures, Phys. Rev. B 78 (13) (2008) 134106.

[43] H.J. Monkhorst, J.D. Pack, Special points for Brillouin-zone integrations, Phys. Rev. B 13 (12) (1976) 5188.

[44] O. Arnold, J.-C. Bilheux, J. Borreguero, A. Buts, S.I. Campbell, L. Chapon, M. Doucet, N. Draper, R.F. Leal, M. Gigg, V. Lynch, A. Markvardsen, D. Mikkelson, R. Mikkelson, R. Miller, K. Palmen, P. Parker, G. Passos, T. Perring, P. Peterson, S. Ren, M. Reuter, A. Savici, J. Taylor, R. Taylor, R. Tolechenov, W. Zhou, J. Zikovsky, Mantid – data analysis and visualization package for neutron scattering and $\mu$ SR experiments, Nuclear Instrum. Methods Phys. Res. Sect. A 764 (2014) 156–166.

[45] K. Dymkowski, S.F. Parker, F. Fernandez-Alonso, S. Mukhopadhyay, AbINS: The modern software for INS interpretation, Phys. B 551 (2018) 443–448.

[46] B. Rao, P. Jena, Switendick criterion for stable hydrides, Phys. Rev. B 31 (10) (1985) 6726.

[47] D. de Fontaine, The number of independent pair-correlation functions in multicomponent systems, J. Appl. Crystallogr. 4 (1) (1971) 15–19.

[48] M.M. Nygård, W. Sławiński, G. Ek, M.H. Sørby, M. Sahlberg, D. Keen, B. Hauback, Local order in high-entropy alloys and associated deuterides – a total scattering and Reverse Monte Carlo study, Acta Mater. 199 (2020) 504–513.

[49] E. Pickering, N. Jones, High-entropy alloys: a critical assessment of their founding principles and future prospects, Int. Mater. Rev. 61 (3) (2016) 183–202.

[50] L. Owen, H. Stone, H. Playford, The assessment of local lattice strains in alloys using total scattering, Acta Mater. 170 (2019) 38–49.

[51] P.C.H. Mitchell, S.F. Parker, A.J. Ramirez-Cuesta, J. Tomkinson, Vibrational Spectroscopy with Neutrons – with Applications in Chemistry, Biology, Materials Science and Catalysis, Series On Neutron Techniques And Applications, World Scientific Publishing Company, 2005.

[52] C.-Z. Wang, R. Yu, H. Krakauer, First-principles calculations of phonon dispersion and lattice dynamics in La2CuO4, Phys. Rev. B 59 (14) (1999) 9278.

[53] X. Ke, A. Kuwabara, I. Tanaka, Cubic and orthorhombic structures of aluminum hydride $AlH_3$ predicted by a first-principles study, Phys. Rev. B 71 (18) (2005) 184107.

[54] P. Vajeeston, P. Ravindran, H. Fjellvg, Phonon, IR, and Raman spectra, NMR parameters, and elastic constant calculations for $AlH_3$ polymorphs, J. Phys. Chem. A 115 (39) (2011) 10708–10719.

[55] Ø. S. Fjellvåg, J. Armstrong, P. Vajeeston, A.O. Sjåstad, New insights into hydride bonding, dynamics, and migration in $La_2LiHO_3$ oxyhydride, J. Phys. Chem. Lett. 9 (2) (2018) 353–358.